Indian Journal of Engineering & Materials Sciences
Vol. 33, February 2026, pp. 68-86
DOI: 10.56042/ijems.v33i01.20147

Advancing sustainability with the integration of PV-wind system for electric vehicle charging with optimized MPPT hybrid DC-DC converter

Tharwin Kumar Ravi Kumar[a,*] & Christober Asir Rajan Charles Gnanakkan[b]

[a,b]Department of Electrical and Electronics Engineering, Puducherry Technological University, Puducherry 605014, India

[a]Department of Electrical and Electronics Engineering, Mohan Babu University, Tirupati 517 102, Andhra Pradesh, India.

Received: 28 May 2025; accepted: 06 November 2025

The accelerated adoption of electric vehicles (EVs) has improved fuel efficiency and eco-friendly transportation, yet it has also introduced challenges, notably the strain on power grids during peak hours. To address this issue, the proposed research has integrated hybrid renewable energy resources (HRESs) with EV charging. The research has focused on the fusion of hybrid energy system that has combined solar, wind and battery technologies. The novel aspect of this work has involved the implementation of an Improved zeta-cuk (IZC) converter, supported by a cascaded adaptive neuro-fuzzy inference system (ANFIS) for maximum power point tracking (MPPT). The proposed bidirectional switched inductor (SL) based improved zeta-cuk converter has enhanced system efficiency, stability and adaptability of PV-based EV charging. This setup has aimed to improve and stabilize the steady-state voltage at the converter output. Additionally, wind system utilizing doubly fed induction generator (DFIG) has been introduced. A proportional integral (PI) controller has ensured stable voltage levels across various operational scenarios. The grid system has been incorporated as a complementary power source, providing electricity when the output from RES has been insufficient. A novel adaptive hybrid control (AHC) algorithm has been developed to manage power flow and EV battery charging by switching between PV, WECS and grid power. The validation process has been carried out using MATLAB revealing a converter efficiency of 95.86%, coupled with a notable reduction in total harmonic distortion (THD) to 2.34%, confirming the effectiveness and feasibility of proposed hybrid energy system.

Keywords: Cascaded ANFIS MPPT, DFIG-wind system, HRES, Improved zeta-cuk (IZC) converter, PV system

1 Introduction

The surge in popularity of EVs is primarily driven by their superior fuel efficiency and environmentally friendly operation, Li[1]. Unlike traditional fossil fuel vehicles, EVs contribute to reduced carbon emissions and a greener transportation ecosystem, Lenka[2]. However, this rising adoption of EVs also brings forth a distinctive set of challenges, while charging. Simultaneously advancing renewable power generation and EV technology proves effective in reducing EVs' emissions, fostering renewable energy adoption, and promoting sustainable energy use worldwide, Gomathi[3]. Among the diverse components of HRES, solar PV and wind power technologies serve pivotal roles in reshaping EV charging landscape Bekiroglu[4]. The integration of HRES, PV, and wind for EV charging signifies a transformative paradigm in which clean energy sources converge to address the dual challenges of reducing carbon emissions and stimulating viable transport, Kavin[5].

The integration of renewable energy sources (RES) holds great promise for sustainable power generation. One such system combines wind energy, utilizing DFIG Velpula[6], with PV technology to create a robust energy infrastructure. The integration of DFIG allows for dynamic control of power generation, Xia[7], making it well-suited for applications like EV charging. The combination of wind and solar sources provides a continuous and reliable power supply, contributing to the sustainability of the EV charging infrastructure. In a PV-based system, DC-DC converters Pires[8] are developed for transforming electrical characteristics of power generated by PV panels. These converters serve a crucial role in adapting direct current (DC) output from PV panels to load or grid requirements, which often operates on alternating current (AC). The Boost converter is a prominent DC-DC converter, which is capable of delivering the higher voltages required by EV power trains, Kumar[9]. However, its main drawback is the lack of bidirectional operation, which limits their adaptability in scenarios requiring both charging and discharging of batteries.

---

*Corresponding author (E-mail: tharwinkumar@ptuniv.edu.in)

Additionally, its sensitivity to input voltage fluctuations, causes inefficiency under variable PV condition, Preethy[10]. Buck-Boost converter, on the other hand, provide flexibility to both step up and step down voltage, making it adaptable for varying power requirements. However, Buck-Boost converter tend to have higher switching losses and introduce additional stress on components, thereby reducing the efficiency and reliability in long-term PV operations, Kumar[11-12]. Zeta converter offer a stable output with low ripple, which is valuable for PV applications that require consistent voltage levels for reliable EV charging. It also supports bidirectional power flow, thereby enhancing flexibility when integrating energy storage with PV systems. Cuk converter, like Zeta converter, provide bidirectional power flow and maintain continuous input and output currents, which is beneficial for reducing stress on PV modules and improving battery management in the EV system, Kumar[13]. Table 1 summarizes the evaluation of some of the recent DC-DC converter topologies.

For subduing the shortcoming of mentioned converters, development of improved converter designs becomes essential. Therefore, a novel improved zeta-cuk converter that overcomes the limitations of existing topologies is presented and discussed in this research. The introduced bidirectional integrated converter design, combines the benefits of both zeta and cuk converter and is based on switched inductor (SL) topology. This unique design enhances power flow flexibility, rendering it ideal for PV-based EV charging systems where both charging and discharging capabilities are essential.

The PV system integration with MPPT serves a pivotal purpose in optimizing PV power output. Numerous researchers have put forth various algorithms and artificial intelligence techniques for determining MPPT of PV systems, Ibrahim[20]. Among the widely recognized algorithms employed in this context are perturb and observe method, Bhan[21], incremental conductance method, Gupta[22]. These approaches are characterized by their simplicity of implementation and reliance on duty cycle adjustments in small increments, but these conventional techniques often exhibit slower response times and struggle to adapt quickly to dynamic environmental changes. In recent times, several researchers have devised modified MPPT, Ali[23] algorithms tailored for various applications, providing advancements beyond traditional methods. In reference Allahabadi[24], artificial neural networks (ANN) in achieving fast and accurate maximum Power Point (MPP) tracking is proposed, showcasing faster convergence speeds and slight oscillations around the MPP. The study recommends implementing a fuzzy logic controller (FLC)-based MPPT Subramanian[25] approach in DC microgrids, which offer superior response time and accuracy, contributing to the efficiency of the DC

Table 1 — Summary of DC-DC converters.

Author/Year/Reference	Converter	Merits	Demerits	Applications
Konstantinos Zaoskoufis *et al*, 2020 Zaoskoufis[14]	Improved Boost-Based High Step-Up Converter	Enhanced efficiency, reduced size and achieves higher DC voltage gains	Suitable only for integration with low MPP voltage PV modules in DC microgrid setups.	DC microgrid applications
Ahmed Shawky *et al*, 2021 Shawky[15]	Improved SEPIC	Input current continuity with voltage boosting and buck functionality	Increased sensitivity to component mismatches.	Grid-tied applications with RES.
MummadiVeerachary *et al*, 2021 Veerachary[16]	Enhanced Gain Buck-Boost	Quadratic buck-boost voltage transformation.	Additional buck stage required for true quadratic conversion	Power electronics, voltage regulation
Arup Ratan Paul *et al*, 2021 Paul[17]	SEPIC-Cuk	Single stage, transformer-less design for better power evacuation	Limited scalability due to single high-frequency switch	Residential solar installations, small-scale PV systems
Yangbin Zeng *et al*, 2021 Zeng[18]	Capacitor Clamped DC-DC Converter	Addresses need for high voltage gain in photovoltaic cells.	Scalability due to the reliance on a single high-frequency switch	Applications with low output voltage sources
Seyed Hossein Hosseini *et al*, 2021 Hosseini[19]	Quadratic Bidirectional	Improved voltage transfer ratio for both directions of current.	High-frequency switching operations	Tailored specifically used for charging/discharging of EV.

microgrid. FLCs exhibit sensitivity to variations, potentially affecting their performance in certain situations. The paper Ibrahim[26] introduces an ANFIS-MPPT technique for a reconfigurable solar based battery charger. Compared to conventional MPPT schemes, the higher accuracy, faster response, and improved tracking efficiency is accomplished, but complexity arises in implementing ANFIS. These techniques leverage sophisticated optimization algorithms such as particle swarm optimization (PSO) Kraiem[27], genetic algorithm (GA) Abadlia[28], ant colony optimization (ACO) Huang[29], and grey wolf optimization (GWO) Guo[30], to overcome the limitations related to inaccurate training complexity. Each algorithm brings unique advantages to MPPT process, however, their computational complexity poses challenges, impacting processing time and energy consumption. Striking a balance between algorithm benefits and limitations is essential for resilient and efficient renewable energy systems. Through a critical examination of existing literature, emerging trends, and case studies, this research strives to contribute valuable insights into the effectiveness, challenges, and future prospects of HRES-based EV charging. The contribution of proposed work involves:

- Integration of HRESs addresses challenges in EV adoption, specifically strain on power grids during peak hours.
- Introduction of improved zeta-cuk (IZC) converter and cascaded ANFIS for MPPT enhances stability and efficiency of energy conversion.
- Incorporation of wind system with DFIG managed by PI controller adds versatility to operational scenarios.
- The incorporation of a novel AHC algorithm to control the EV battery charging by managing the power flow. The AHC algorithm prioritizes renewable sources and optimizes charging efficiency by adjusting the power path according to EV battery’s state of charge (SOC) and availability of power sources.
- Validation through MATLAB simulations underscores practicality and effectiveness of proposed hybrid energy system.
- Overall, the research provides a comprehensive and sustainable solution for EV charging, combining various renewable energy sources and advanced control systems.

2 Materials and Methods

The system combines solar, wind, and battery technologies to enhance the proficiency, consistency, and sustainability of energy generation and utilization. IZC converter is implemented for improving PV voltage. The converter is complemented by a cascaded ANFIS approach designed for tracking of MPPT. Furthermore, the research introduces a wind energy system featuring DFIG that allows for variable speed operation, providing flexibility in adapting to changing wind conditions. The equivalent configuration of proposed HRES based EV charging system depicted in Fig. 1. To manage the DFIG and

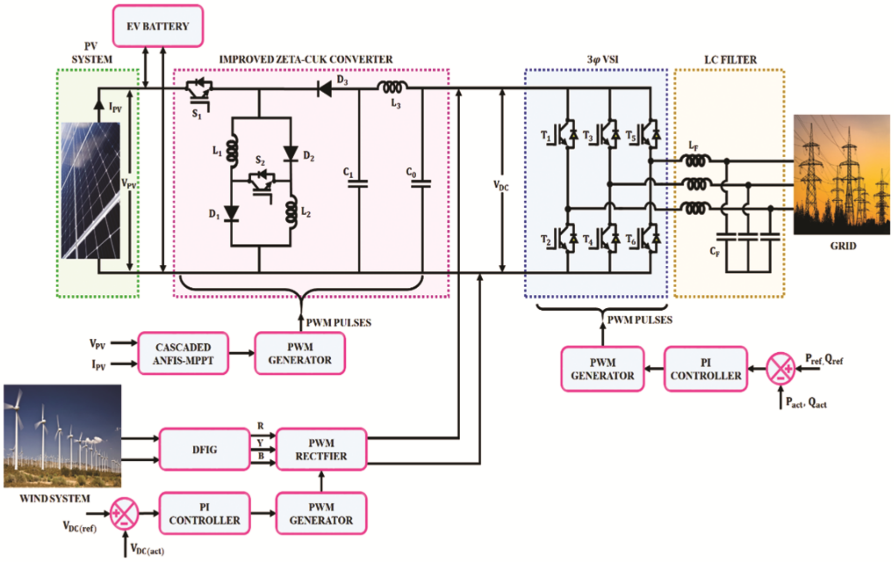

Fig. 1 — Proposed HRES based EV charging configuration.

ensure stable voltage levels across various operational scenarios, a PI controller is employed.

The controller dynamically adjusts the electrical characteristics of DFIG, optimizing its performance and subsidizing to overall stability of hybrid system. The direct connection of EV battery to DC link allows for smooth charging when adequate renewable energy is available, while the converter's design minimizes voltage ripple and enhances power stability, even under changing environmental inputs. The battery is capable of handling voltage disturbances of ±10%, ensuring resilience and stability in operation. This tolerance allows the battery to adapt to minor fluctuations in the DC link voltage caused by varying renewable energy inputs or load changes. In addition to charging, the setup supports discharging of excess energy to the grid. This is achieved through a three-phase VSI, which converts the DC power from the Zeta-Cuk converter into three-phase AC. An LC filter is used to smooth the inverter output, minimizing THD and producing a high-quality AC signal suitable for grid injection. The VSI's operation is controlled by a PI controller. The dual functionality of the charging station maximizes energy utilization and reduced the reliance on conventional grid power.

2.1 EV charging station

The proposed EV charging station setup utilizes HRES consisting of PV system and DFIG-based WECS to charge the EV battery and supply power to the grid. The system's operation involves several modes based on the availability of renewable power sources and EV battery charging demands. When the EV battery requires charging and sufficient solar power is available, the PV system supplies energy directly to the battery. In cases where no EV is connected for charging at the station, the PV generated energy is boosted using the IZC converter and then supplied to the grid. When the PV system is unavailable, power from WECS is supplied to the EV battery through the IZC converter to ensure consistent charging. When both PV and WECS power sources are unavailable, the system draws power from the grid to charge the EV battery. This grid power is stepped down using the IZC converter to match the EV battery's charging requirements, ensuring the battery is charged even in the absence of renewable sources. To efficiently manage power flow and charging, a novel Adaptive Hybrid Charging (AHC) algorithm is proposed that adjusts current paths based on RESs availability, the state of the EV battery, and grid conditions. The algorithm prioritizes renewable sources over the grid, optimizes power flow to the battery, and ensures that excess power is routed to the grid when no EV is connected for charging. The Pseudocode of AHC is,

Algorithm 1: AHC algorithm

```
Initialize system parameters and power thresholds
Monitor PV power availability,
WECS power availability, and grid power
Monitor EV battery state of charge (SOC) and charging status (EV_Charging)
While system is active:
    If EV_Charging is TRUE:
        If P_PV > Minimum_PV_Power:
            // Charge battery with PV power
            Supply boosted power to EV battery
        Else If P_WECS > Minimum_WECS_Power:
            // Charge battery with WECS power via IZC converter
            Convert WECS AC power to DC using PWM rectifier
            Supply converted power to EV battery via IZC converter
        Else:
            // Charge battery with grid power via IZC converter
            Step down grid power using IZC converter
            Supply stepped - down power to EV battery
        End If
    Else:
        If P_PV > Minimum_PV_Power:
            // Supply PV power to grid via IZC converter and VSI
            Boost PV power using IZC converter
            Convert boosted DC to 3 - phase AC via VSI
            Filter AC power and supply to grid
        Else If P_WECS > Minimum_WECS_Power:
            // Supply WECS power to grid via VSI
            Convert WECS AC power to DC using PWM rectifier
            Combine with DC link and supply to grid via VSI
        End If
    End If
    // Priority switching in case of fluctuating conditions
    If P_PV drops below threshold during charging:
        Switch to WECS or grid power if available
    Else If $P_{WECS}$ drops below threshold during charging:
        Switch to grid power if PV and WECS are both unavailable
    End If
    Update SOC and log power flows for monitoring
End While
```

The work flow of AHC algorithm is provided in Fig. 2. Hence, by adapting to fluctuating power availability, the AHC algorithm provides a reliable

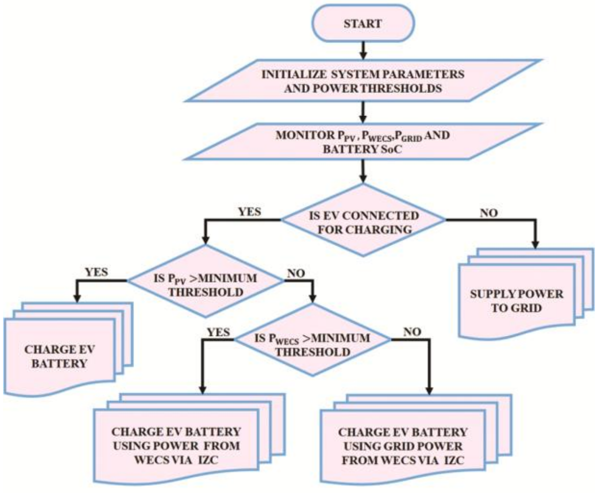

Fig. 2 —Workflow of AHC algorithm.

and sustainable solution for EV charging, using renewable sources while maintaining grid stability.

2.2 Design of PV system

Solar photovoltaic cells are formulated with various models. Nevertheless, this work opts for the most straightforward and essential equivalent circuit configuration for solar cell. This configuration contains a current source operating in parallel with diode and shunt resistor. The schematic representation of this circuit is depicted in Fig. 3, serving as the adopted model for this research. This circuit will be subsequently translated into mathematical equations to facilitate analysis and characterization.

The generated current I_{ph} by PV panel is intricately connected to several parameters associated with the solar cell. These parameters include the series resistance R_{series}, parallel shunt resistance R_{shunt}, solar cell output voltage V_{pv}, and diode saturation current I_0. The relationship among these parameters is mathematically expressed in the following equation:

$$I_{pv} = N_p I_{ph} - N_p I_0 \left[e^{\frac{q(N_p V_{pv} + N_s R_{series}\, I_{pv})}{\alpha k T\, N_s N_p}} - 1 \right] - \frac{N_p V_{pv} + N_s R_{series}\, I_{pv}}{N_s R_{shunt}} \quad \ldots (1)$$

In this context, I_{ph} represents the current produced by light, I_0 stands for saturation current, k is Boltzmann constant, q designates electron charge, α represents ideality factor within the range of 1 to 2, T signifies the cell temperature measured in Kelvin (K), while N_s and N_p are indicative of number of cells organized in series and parallel, respectively.

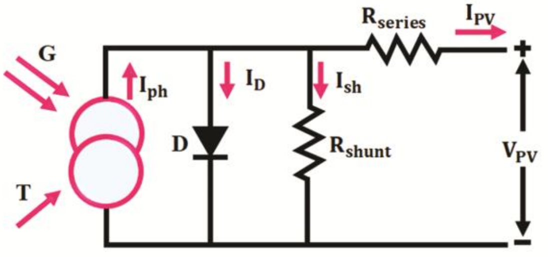

Fig. 3 — Design of PV cell.

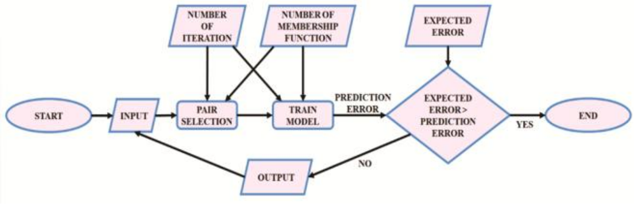

Fig. 4 — Flow chart representation of cascaded ANFIS MPPT.

2.3 Cascaded ANFIS MPPT approach

In the field of PV systems to optimize the extraction of power from solar panels MPPT approaches are implemented. Cascaded ANFIS approach is utilized in this work employing a combination of ANFIS and a cascaded structure, designed to track MPP under changing conditions. Figure 4 illustrates flow diagram of cascaded ANFIS MPPT approach. This approach involves the use of multiple ANFIS structures arranged in a cascaded or sequential manner. Each ANFIS structure in cascade refines the MPPT output of preceding one, contributing to a more accurate and responsive tracking of MPP. The cascaded structure allows for iterative optimization and adjustment of the control parameters, leading to improved performance in dynamically changing conditions.

2.3.1 Input module

The fundamental inputs for module are solar irradiance (G) and temperature (T) that significantly influence the performance of PV. By incorporating these raw inputs at the outset, the cascaded ANFIS MPPT technique is assured to systematically analyze the MPP under diverse conditions.

2.3.2 Pair selection

Its primary objective is to discern the most impactful combinations of input variables, such as solar irradiance and temperature, influencing the MPPT process. Employing a Sequential Feature Selection (SFS) process, the module systematically explores diverse pairs of input variables to identify the combination that optimally influences the MPPT algorithm. Facilitated by a two-input one-output

ANFIS model, this module assesses the impact of different input variable pairs on MPPT output. Through the calculation of Root Mean Square Error (RMSE) and predicted output (Y) for each pair, the ANFIS model quantifies the accuracy of predictions, with the best match determined by pair yielding the lowest RMSE. The final output is the identification of this best-matched pair, crucial for predicting MPPT setting under prevailing conditions. This pair is subsequently passed to the Training Module, contributing to the development of a robust MPPT algorithm capable of efficiently tracking the MPP across varying environmental conditions within a PV system.

2.3.3 Training module

The initial step involves pairing input variables, such as solar irradiance and temperature, with the best-matched combination determined by the Pair Selection Module. Subsequently, the two-input ANFIS model generates two crucial outputs: RMSE and predicted output (Y). The equation for RMSE involves the summation of the squared differences between actual (A) and predicted (P) values across all data points, normalized by sample size (N). This calculation provides an assessment of the accuracy for ANFIS model's predictions.

$$RMSE = \sqrt{(A-P)^2} \qquad \text{... (2)}$$

$$RMSE = \left[\sum_{i=1}^{N} \frac{(O_{Ai} - O_{Pi})^2}{N}\right]^{\frac{1}{2}} \qquad \text{... (3)}$$

Concurrently, the fuzzy rule for predicted output (Y) is established through a weighted sum of the fuzzy sets corresponding to input variables. The weights (w_1, w_2)represent the significance assigned to (f_1, f_2)–fuzzy sets encapsulate the linguistic terms associated with the input variables. They are accomplished using

$$f = \frac{w_1}{w_1+w_2} f_1 + \frac{w_2}{w_1+w_2} f_2 \qquad \text{... (4)}$$

This fuzzy rule effectively captures the intricate relationships between the input variables an MPPT output, contributing to the adaptability and responsiveness of ANFIS model.

2.3.4 Iteration

The iterative process in cascaded ANFIS progressively refines the MPPT algorithm for PV systems. After the initial two-input ANFIS model in the Train Module, outputs from the first iteration (Y_1, Y_2) inform the subsequent iteration, fine-tuning the algorithm. Iterations continue until a target error is reached. With each iteration, the ANFIS model adjusts parameters using feedback from prior outputs, enhancing precision and adaptability to environmental changes. Termination conditions balance precision and computational efficiency, contributing to a robust MPPT strategy that maximizes energy harvesting efficiency in diverse conditions.

2.3.5 Fuzzy rules

The establishment of fuzzy rules in the context of cascaded ANFIS MPPT technique is a critical step that delineates the relation between input variables and MPPT output in linguistic terms. Figure 4 provides an example illustration of train module.

Here in Table 2 and 3, specific rule table for cascaded ANFIS MPPT involves defining fuzzy rules based on input variables and MPPT output is listed with linguistic variables Low, Medium and High.

In a cascaded ANFIS MPPT system, multiple ANFIS structures is connected in series. Each ANFIS structure refines the output of previous one, allowing for more precise MPPT. The output of the first ANFIS structure becomes one of inputs to the next one.

This is final output of ANFIS system and represents the estimated MPPT. The controlled output using Cascaded MPPT from the controller is fed converter switches.

2.4 Proposed improved zeta-cuk(IZC) converter

The IZC shown in Fig. 5 is an enhancement of traditional Zeta-Cuk Converter, which aims to address

Table 2 — Rule Table for ANFIS 1.

Rule	Solar Irradiance (G)	Temperature (T)	Predicted Output (Y)
1	Low	Low	Low
2	Low	Medium	Low
3	Low	High	Medium
4	Medium	Low	Low
5	Medium	Medium	Medium
6	Medium	High	High
7	High	Low	Medium
8	High	Medium	High
9	High	High	High

Table 3 — Rule Table for ANFIS 2.

Rule	MPPT Output (from ANFIS 1)	MPPT Output (ANFIS 2)
1	Low	Low
2	Medium	Medium
3	High	High

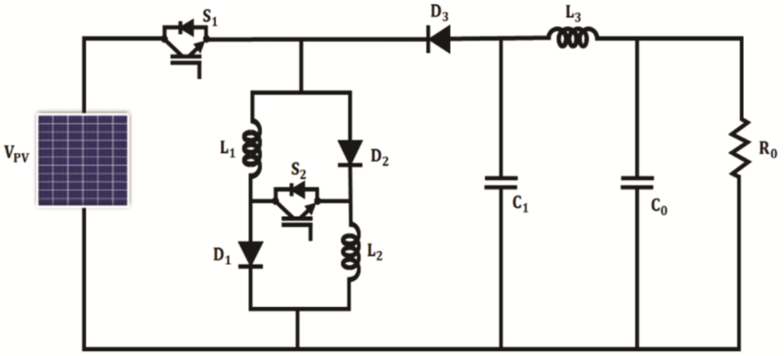

Fig. 5 — Proposed IZC converter.

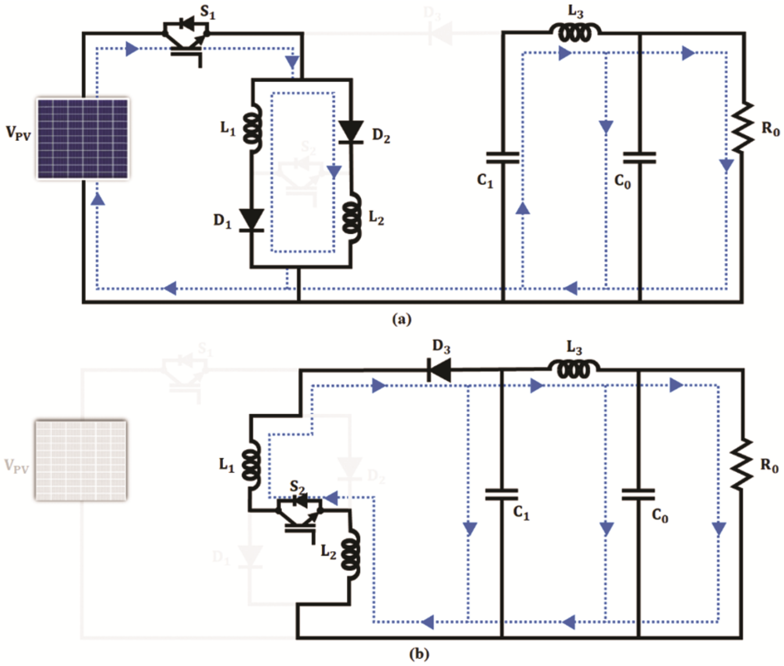

Fig. 6 — Operational characteristics of IZC (a) at Mode 1 and (b) at Mode 2.

certain limitations and improvedactions, in terms of efficiency, reduce stress on components, and to provide better transient response.

2.4.1 Operational characteristics

Mode 1 initiates when switch S_1 is activated, withS_2 in OFF state. The current follows the path outlined in Fig. 6(a). In this mode, inductors L_1 and L_2 undergo charging through diodes D_2 and D_1, respectively. Simultaneously, capacitors C_1 and L_3 experience charging through the load. Diode D_2 assumes a reverse bias owing to its lower potential. Throughout this phase, output capacitor C_0 accumulates and stores energy. On applying Kirchhoff's Voltage Law (KVL) to the inductor L_1 and L_2, the expression becomes,

$$V_{L_1} = V_{L_2} = V_{PV} \quad \text{... (5)}$$

The output voltage of proposed IZC converter in Mode 1 is expressed as,

$$V_{out} = V_{PV} = V_{C_1} \quad \text{... (6)}$$

The inductors L_1 and L_2current while charging is related to inductance and voltage as follows:

$$I_{L_1} = \frac{1}{L_1}\int V_{L_1} dt \quad \text{... (7)}$$

$$I_{L_2} = \frac{1}{L_2}\int V_{L_2} dt \quad \text{... (8)}$$

The current through capacitor C_1 is related to rate of change of charge:

$$I_{C_1} = C_1 \frac{dV_{C_1}}{dt} \quad \text{... (9)}$$

Mode 2 commences when switch S_1 is in OFF position with S_2 in ON state, as illustrated in Fig. 6(b). Diodes D_1 and D_2 are deactivated due to their lower potentials, while diodes D_3 assume a forward bias owing to their higher potential points. In this phase, both inductors L_1 and L_2 initiate the discharge of energy through diode D_2. Consequently, the switching voltage stress is mitigated by C_1 and D_3. The energy demanded by the load is supplied by output capacitor C_0. Figure 7 demonstrates the switching waveform of IZC converter.

By employing KVL, the ensuing equations are deduced.

$$V_{L_1} + V_{L_2} = V_{PV} - V_{C_1} \quad \text{... (10)}$$

According to volt–second balance theory under steady-state conditions, the capacitor voltage,V_{C_1} is articulated as follows.

$$V_{C_1} = V_{PV} + V_{D_2} + V_{D_1} \quad \text{... (11)}$$

$$V_{D_2} = V_{D_1} = \frac{D}{1-D} V_{PV} \quad \text{... (12)}$$

On substituting Expression (11) and (12) in (6), the expression becomes

$$V_0 = V_{PV} + V_{PV} + \frac{D}{1-D} V_{PV} + \frac{D}{1-D} V_{PV} \quad \text{... (13)}$$

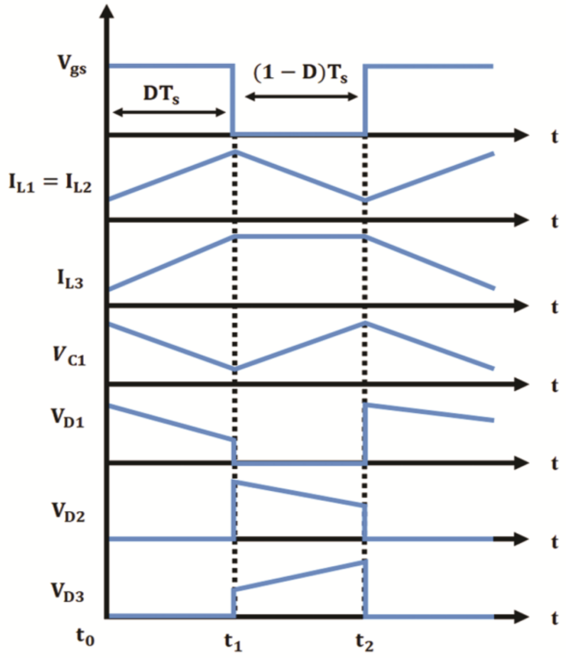

Fig. 7 — Switching characteristics of IZC converter.

$$V_0 = 2V_{PV} + \frac{2D}{1-D} V_{PV} \quad \text{... (14)}$$

$$V_0 = 2V_{PV} \left(1 + \frac{D}{1-D}\right) \quad \text{... (15)}$$

$$G_{Boost} = \frac{V_0}{V_{PV}} = \left(\frac{2}{1-D}\right) \quad \text{... (16)}$$

2.4.2 Analysis of voltage and current stress

The voltage supplied to the switch is computed in the following manner:

$$V_s = \frac{V_{PV}}{(1-D)} \quad \text{... (17)}$$

The voltage applied across diodes during ON condition of switch is expressed as

$$V_{D_2} = \frac{DV_{PV}}{(1-D)} \quad \text{... (18)}$$

$$V_{D_1} = V_{D_3} = V_{PV} \quad \text{... (19)}$$

The voltage applied across diodes during OFF condition of switch is expressed as

$$V_{D_1} = \frac{DV_{PV}}{(1-D)} \quad \text{... (20)}$$

$$V_{D_3} = V_{PV} \quad \text{... (21)}$$

The capacitor voltage stress is written as

$$V_{C_1} = V_{PV} + V_{D_2} + V_{D_1} \quad \text{... (22)}$$

$$V_{C_1} = V_{PV} + \frac{DV_{PV}}{(1-D)} + \frac{DV_{PV}}{(1-D)} \quad \text{... (23)}$$

The average charging current over inductors L_1 and L_2 in Mode 1 is given by:

$$I_{L_1} = \frac{V_{PV} D}{2L_1 f} \quad \text{... (24)}$$

$$I_{L_2} = \frac{V_{PV} D}{2L_2 f} \quad \text{... (25)}$$

The average discharging current through inductors L_1 and L_2 in Mode 2 is given by:

$$I_{L_1} = \frac{V_{PV}(1-D)}{2L_1 f} \quad \text{... (26)}$$

$$I_{L_2} = \frac{V_{PV}(1-D)}{2L_2 f} \quad \text{... (27)}$$

Here, f is the switching frequency.

2.4.3 Efficiency analysis

Efficiency is a crucial metric in power electronics and conversion systems as it quantifies the ratio of output power to input power. The efficiency analysis of Proposed IZC Converter is conducted to assess how effectively the converter convert electrical power while minimizing energy losses. The efficiency (η) of a converter is typically calculated using the formula:

$$\eta = \frac{Output\ \ Power\ \ (P_{out})}{Input\ \ Power\ \ (P_{out})} \times 100\% \qquad \ldots (28)$$

$$\eta = \frac{600V \times 13.9A}{60V \times 145A} \times 100\%$$

$$\eta = 95.86\%$$

The efficiency analysis provides that the performance of IZC converter under varying conditions is observed to be 95.86%. This indicates that a larger proportion of the input power is successfully delivered to output, resulting in reduced energy wastage and increased overall system performance.

2.5 Modelling of WECS & DFIG

The wind turbine's mechanical output power can be expressed using the following equation.

$$P_{Tur} = \frac{1}{2}\rho\pi r^2 C_P(\lambda,\beta)v^3 \qquad \ldots (29)$$

$$Where\ \lambda = \frac{r\omega_m}{v} \qquad \ldots (30)$$

From expressions, tip speed ratio is indicated as λ, speed shaft function is defined as ω_m and C_P specifies power co-efficient of turbine. The torque produced by the turbine is expressed as follows,

$$T_{Tur} = \frac{1}{2}\rho\pi r^2 \frac{C_P(\lambda,\beta)v^3}{\lambda} \qquad \ldots (31)$$

The DFIG is a crucial component in the wind conversion system shown in Fig. 8, offering easy control and enhanced energy output during wind speed variations. It comprises stator and rotor windings, with stator connected to power grid and rotor linked to a power converter for output control. In PARK frame, the electrical equations governing DFIG are expressed by specific equations.

$$V_{ds} = R_s I_{ds} + \frac{d\varphi_{ds}}{dt}\omega_s\varphi_{qs} \qquad \ldots (32)$$

$$V_{qs} = R_s I_{qs}\frac{d\varphi_{qs}}{dt}\omega_s\varphi_{ds} \qquad \ldots (33)$$

Where $\varphi_{ds} = L_s I_{ds} + L_m I_{dr}$ and $\varphi_{qs} = L_s I_{qs} + L_m I_{qr}$

$$V_{dr} = R_r I_{dr}\frac{d\varphi_{dr}}{dt}(\omega_s - \omega)\varphi_{qr} \qquad \ldots (34)$$

$$V_{qr} = R_r I_{dr} + \frac{d\varphi_{qr}}{dt} + (\omega_s - \omega)\varphi_{dr} \qquad \ldots (35)$$

Where $\varphi_{dr} = L_r I_{dr} + L_m I_{ds}$ and $\varphi_{qr} = L_r I_{qr} + L_m I_{qs}$

From Expressions (32), (33), (34) and (35) $R_s$and R_r represent phase resistances of stator and rotor, respectively. The electrical speed, denoted by ω, is defined as $\omega = P_{dfig} - \Omega_{mec}$, where P is a constant. Additionally, stator currents include I_{ds} (direct component) and I_{qs} (quadrature component), while the rotor currents consist of I_{dr} (direct component) and I_{qr} (quadrature component).

The active and reactive powers of stator are expressed as follows

$$\begin{cases} P_s = \frac{3}{2}\left(V_{ds}I_{ds} + V_{qs}I_{qs}\right) \\ Q_s = \frac{3}{2}\left(V_{qs}I_{ds} - V_{ds}I_{qs}\right) \end{cases} \qquad \ldots (36)$$

The torque produced by DFIG is determined by stator currents and rotor flux, as indicated in the given equation.

$$T_{em} = \frac{3}{2}\frac{P_{dfig}M}{L_s}\left(I_{dr}\varphi_{qs} - I_{qr}\varphi_{ds}\right) \qquad \ldots (37)$$

The voltage generated by the wind system, which is successfully obtained through the VSI, undergoes conversion into AC to be utilized by the grid.

3 Results and Discussion

In this section, the results of proposed study, offering comprehensions into performance, efficiency, and environmental impact of integrated PV-Wind system for EV charging is demonstrated using

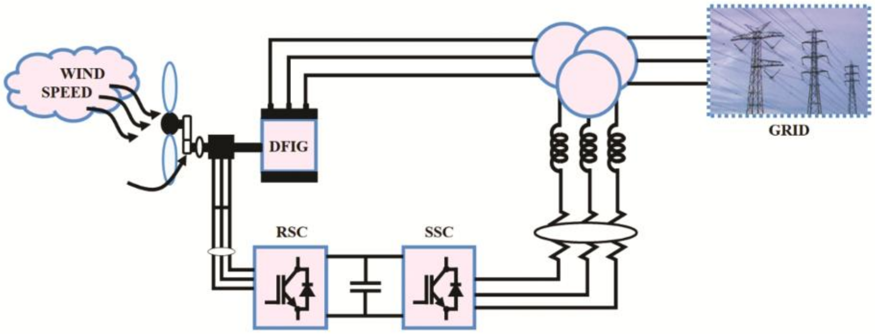

Fig. 8 — DFIG builtwind system.

MATLAB Simulation. Table 4 specifies the design specification parameters of proposed system.

3.1 Case 1: At varying temperature and irradiation

The changing patterns in temperature and irradiance values over time is demonstrated in Fig. 9 (a-b). It is seen that at initial stage a consistent temperature level of $25^{\circ}\mathrm{C}$ is maintained. After $0.15s$, increase in temperature level occurs indicating upsurge at $35^{\circ}\mathrm{C}$ and maintained constant. Similarly, irradiance level of $800W/sq-m$ is observed, while after $0.15s$, the irradiance increases and maintains at $1000W/sq-m$, respectively.

Table 4 — Specification of system components.

Parameter	Rating
Solar PV System	
Total Power	10kW
Open Circuit Voltage	$37.25V$
Short Circuit Voltage	$8.95A$
Peak Power	$150W$
Maximum Peak Current	$8.35A$
Maximum Peak Voltage	$29.95V$
Improved Zeta- Cuk Converter	
L_1,L_2,L_3	$1mH$ 1mH
C_1	4.7μF
C_0	2200μF
Wind Turbine	
No. of Turbines	1 1
Power	10kW
Voltage	$575V$

The waveform depiction of input voltage and current experienced by solar panel over a specific period, is shown in Fig. 10(a-b). In accordance with solar PV behaviour, the voltage is initially observed at $50V$, followed by rise in voltage at $0.15s$, showing higher voltage of $60V$, which is continued further. Meanwhile, the current waveform is observed to be with oscillations, and shows a stabilized current of $145A$ after $0.3s$.

The reaction to input supply from solar PV panel utilized IZC converter in reference with voltage and current is demonstrated in Fig. 11(a-b). With input PV voltage of 60V, the converter responses with minor oscillations at the starting and shows a stabilized voltage value of $600V$ at $0.3s$, without any further distortions. In the meantime, the converter current shows slight oscillations and results with stabilized current of $13.9A$, respectively.

3.2 Case 2: At constant temperature and varying irradiation

Scenario indicating varying intensity and stabilized temperature is illustrated in Fig. 12. From Fig. 12(a) shows stabilized temperature of $35^{\circ}\mathrm{C}$ is accomplished over time, while the irradiation waveform in Fig. 12(b) indicates initial intensity level of $800W/sq-m$ followed by $1000W/sq-m$ after 0.15s.

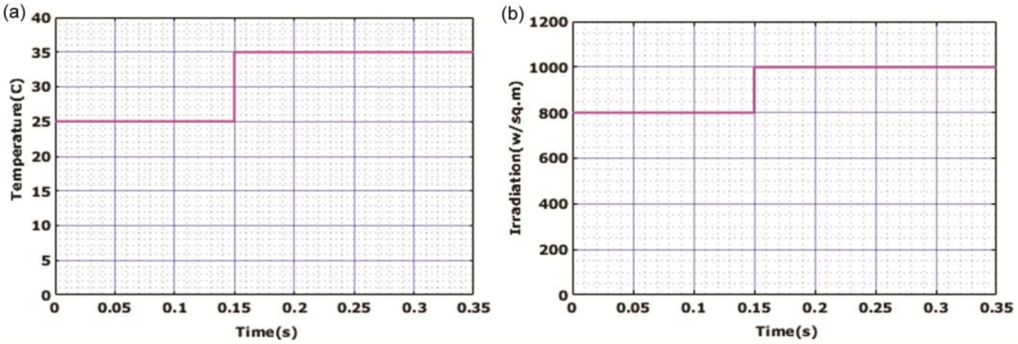

Fig. 9 — Case 1 Illustration of waveform of (a) Solar panel temperature and (b) Irradiance.

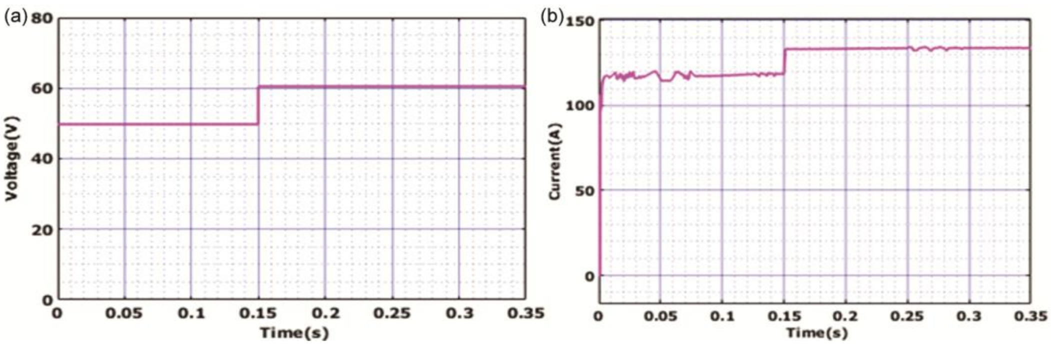

Fig. 10 — Waveform of (a) Voltage and (b) Current for input solar panel.

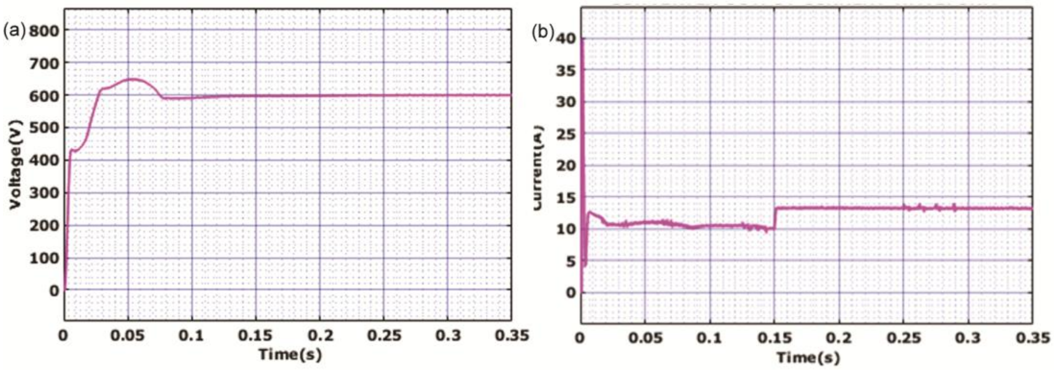

Fig. 11 — Output waveforms of IZC converter (a) Voltage and (b) Current.

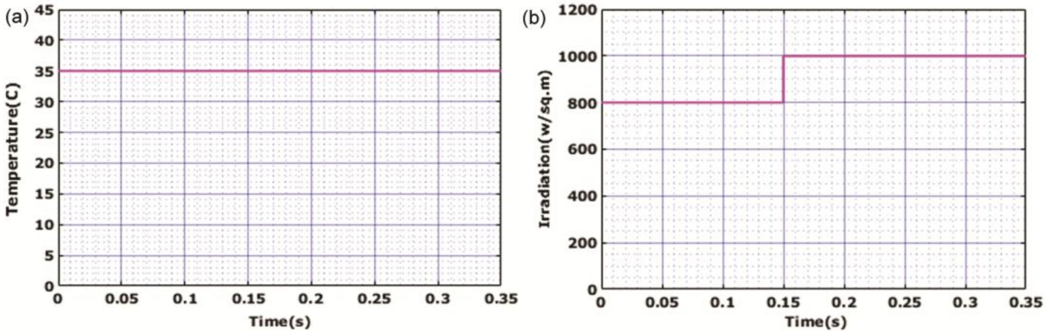

Fig. 12 — Case 2 Illustration with (a) Constant temperature and (b) Varying irradiation.

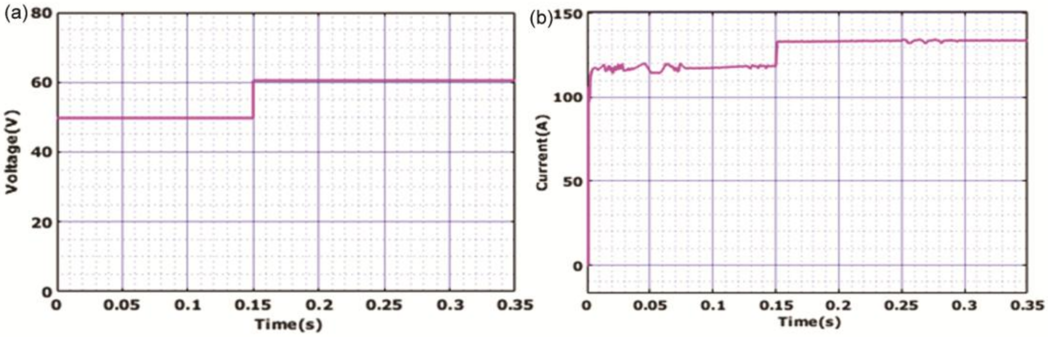

Fig. 13 — Solar panel profile in response to Case 2 scenario (a) Voltage and (b) Current.

The PV panel showcasing initial voltage level of $50V$, accompanied with increase in voltage owing to increase PV profile is illustrated in Fig. 13. It is shown that, the voltage gets increased after $0.15s$ and continues at $60V$ further as in Fig. 13(a). Similarly, oscillation in current is observed and shows settlement after $0.3s$ at $145A$, and maintains stable as in Fig. 13(b).

The converter shows enhanced performance, with boosted voltage level of $600V$ for input PV voltage with $60V$, together with the assistance of cascaded ANFIS MPPT approach as in Fig. 14 (a). Meanwhile, the current shows oscillations at the starting stage and maintain a constant value of $13.9A$, after $0.3s$, as illustrated in Fig. 14(b).

3.3 Case 3: At constant temperature and irradiation

A stabilized temperature and irradiance condition is taken as scenario 3, shown in Fig. 15 to test the converter performance in optimizing the voltage. Notably, the panel is maintained at a temperature of $35°\mathrm{C}$ as in Fig. 15(a) with irradiance level of $1000W/sq$ –as in Fig. 15(b).

In association with, irradiance and temperature profile of scenario 3, the PV panel response is illustrated in Fig. 16. A steady voltage of $60V$ is observed by panel as in Fig. 16(a) with current demonstrating distortions at the earlier stage and settles after $0.3s$, at $145A$ without any additional oscillations as in Fig. 16(b).

For scenario 3 with steady irradiance and temperature, the proposed converter illustrated enhanced performance shown in Fig. 17. With initial variations at the beginning, a stabilized voltage level of $600V$ is accomplished at $0.15s$, in support with cascaded ANFIS MPPT as in Fig. 17(a). Meanwhile, severe fluctuations is noticed at the starting phase, followed by mitigation in oscillations. After $0.3s$, a stabilized current level of $13.9A$ is achieved without any fluctuations further as in Fig. 17(b).

The performance of wind turbine response from generator and rectifier is portrayed in Fig. 18(a-b). It is witnessed that, the DFIG shows increased voltage at the beginning and stabilizes at 600V after 0.15s, and continues. Simultaneously, the rectifier responses with 600V DC supply, utilizing PI controller, with minor distortions at the start up stage.

The performance of battery voltage waveform providing a dynamic representation 60V across the battery terminals with changes over time is illustrated in Fig. 19(a). Simultaneously, the current waveform in Fig. 19(b) illustrates the flow of electric charge into and out of the battery during a specific period.

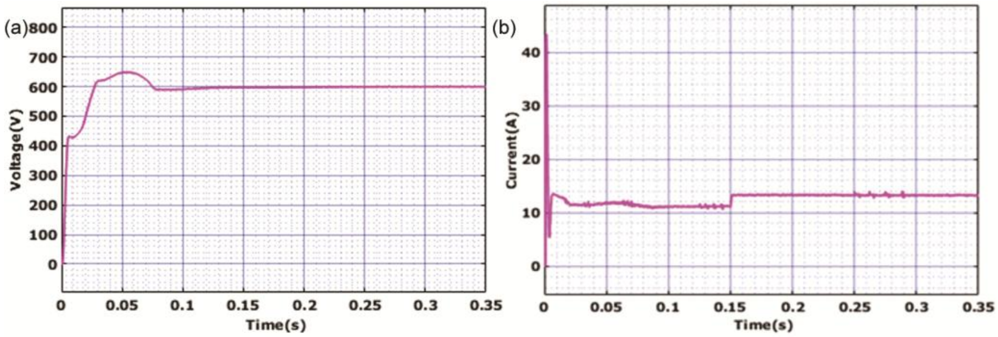

Fig. 14 — Output VI characteristics of improved zeta-cuk converter (a) Voltage and (b) Current.

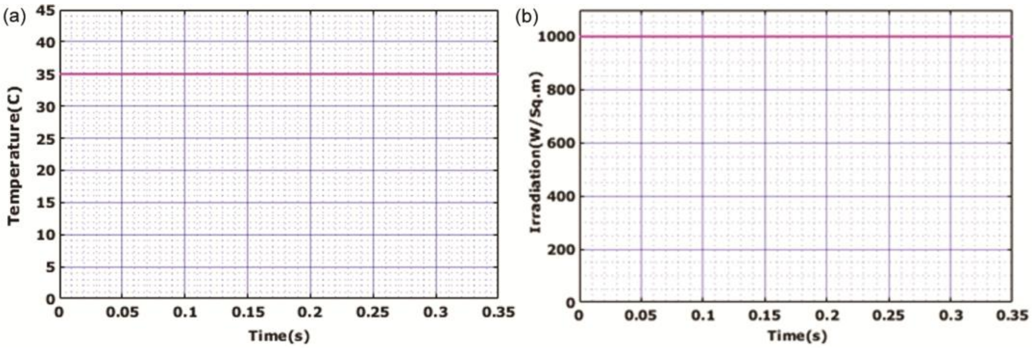

Fig. 15 — Case 3 scenario with (a) steady temperature and (b) Irradiance.

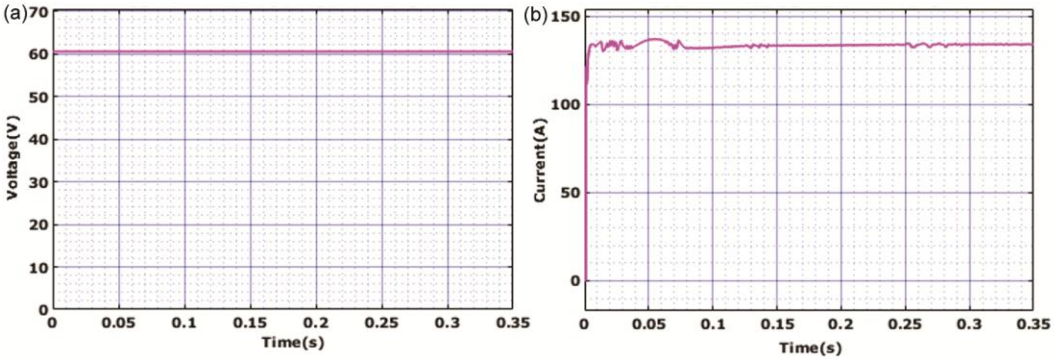

Fig. 16 — Solar panel behaviour to Case 3 (a) Stable temperature and (b) Irradiance.

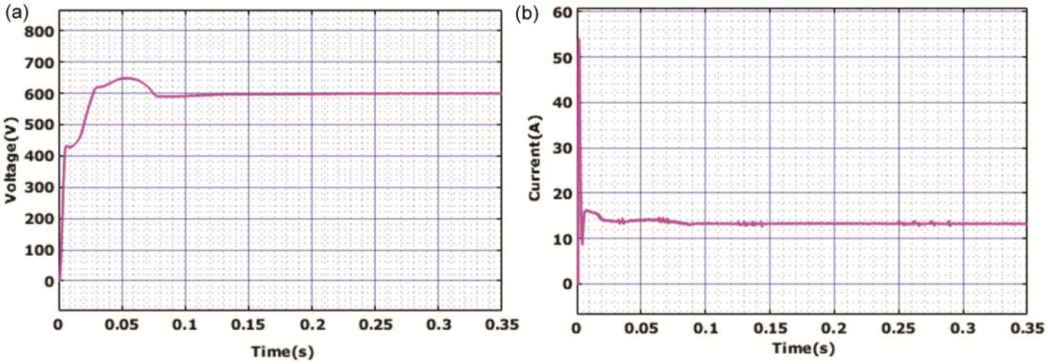

Fig. 17 — Improved zeta cuk converter’s output to Case 3 (a) Voltage and (b) Current.

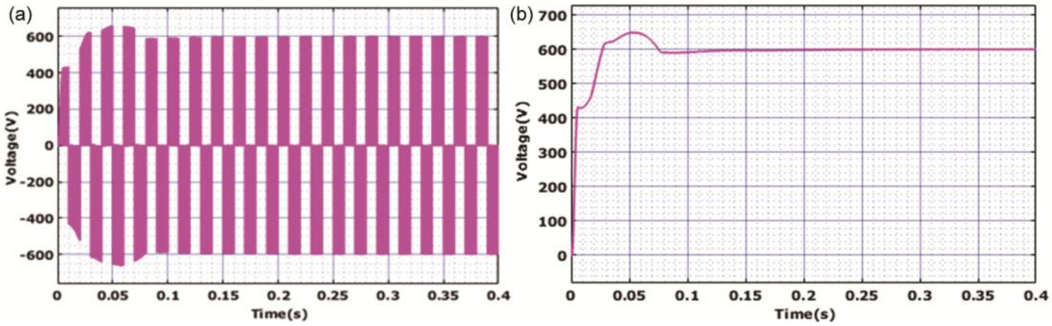

Fig. 18 — (a) DFIG performance and (b) PWM rectifier output.

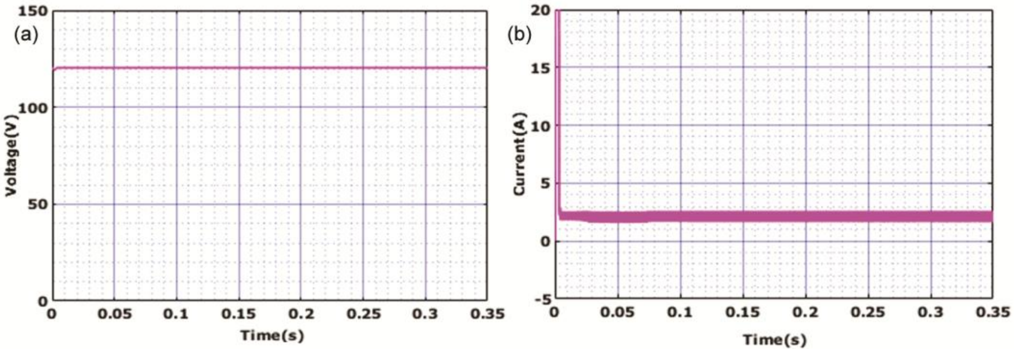

Fig. 19 — Battery profile (a) Voltage and (b) Current waveform.

The SOC of battery, specifically indicating a SOC value of 60% is portrayed in Fig. 20. In this context, an SOC of 60% implies that the battery is holding a charge equivalent to 60% of its total capacity.

The waveform representation shown in Fig. 21(a) and 21(b) highlights a stable grid performance with a steady voltage of $415V$ and a current of $12A$, demonstrating an absence of distortion in the electrical waveforms. This signifies the reliability and steadiness of the grid connection, and supplies a consistent and undisturbed power supply within the integrated system.

Real Power represented in Fig. 22(a), demonstrates the actual power consumed by the system.

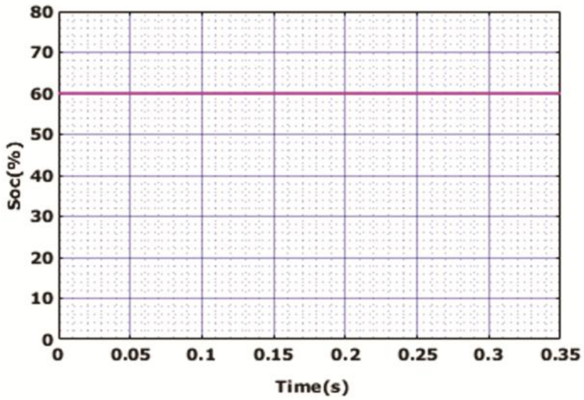

Fig. 20 — State of charge (SOC) of battery.

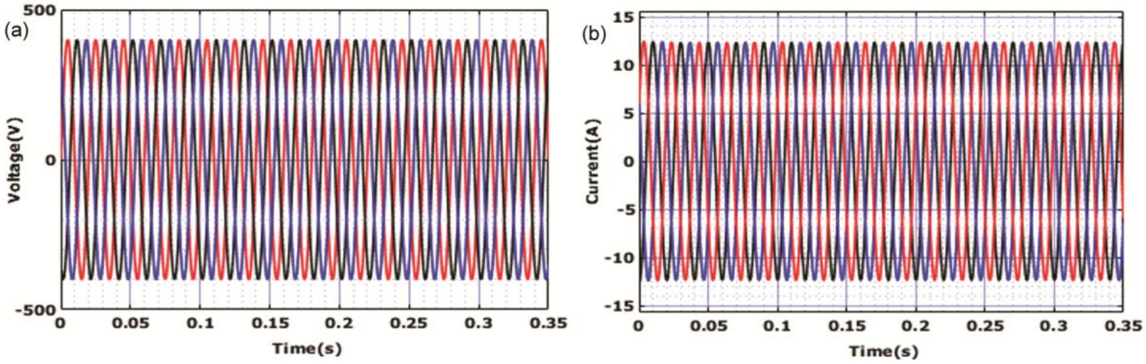

Fig. 21 —Representation of (a) Voltage in grid and (b) Current in grid.

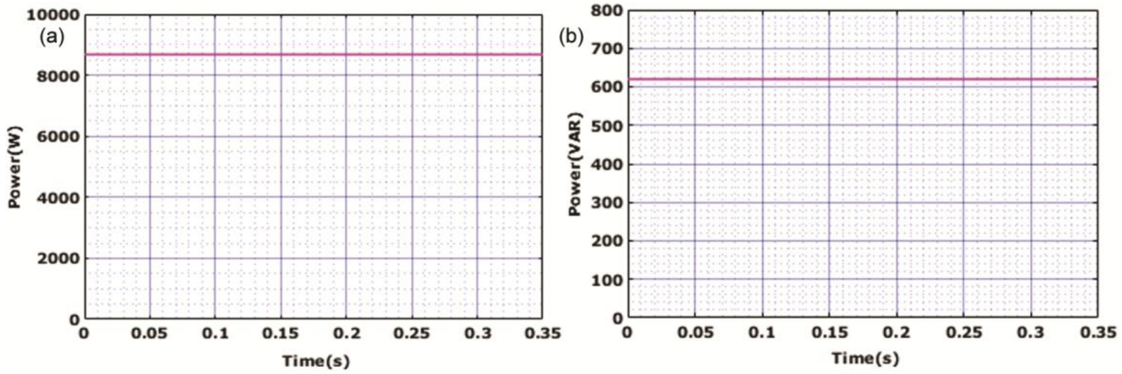

Fig. 22 — Analysis of (a) Real and (b) Reactive power.

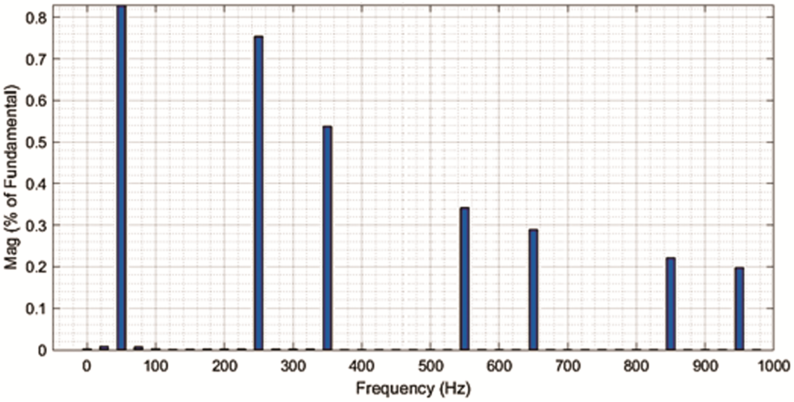

Fig. 23 — THD of grid current.

Simultaneously, Fig. 22(b) illustrates the waveform of reactive power, which represents the non-working power that oscillates between source and load without being consumed. These waveforms helps in identifying potential issues, and improves system efficiency.

The THD represents extent of harmonic components present in current waveform concerning the fundamental frequency. In this context, a THD value of 2.34% is obtained, indicating that the grid current contains harmonics constituting 2.34% of total current, as perceived in Fig. 23. The presented THD of 2.34% suggests that the grid current exhibits a relatively low level of harmonic distortion, contributing to a high-quality power supply.

3.4 Hardware analysis

The hardware configuration depicted in Fig. 24 exemplifies an eco-friendly and adaptable strategy for EV charging, by FPGA control and integration of RESs. Within the hardware arrangement, the controller serves as central control unit, endowed with a cascaded ANFIS MPPT algorithm, designed to efficiently oversee the charging process.

The characteristics of PV Panel through the representation of current and voltage waveforms is presented in Fig. 25(a-b). The visual presentation illustrates the dynamic behaviour of PV panel, showcasing variations in voltage and current over time. An input voltage of $60V$ is sustained, while the current waveform shows $15.3A$ with minor distortion.

The voltage output of IZC converter is demonstrated in Fig. 26(a), revealing enhanced voltage characteristics and a stabilized DC link supply achieved through the implementation of cascaded ANFIS-MPPT algorithm. In parallel, Fig. 26(b) illustrates the current response, initially exhibiting minor oscillations at the beginning and subsequently stabilizing. This behaviour signifies the converter's capability to achieve a steady and controlled current output over time, contributing to overall stability and reliability of DC link supply.

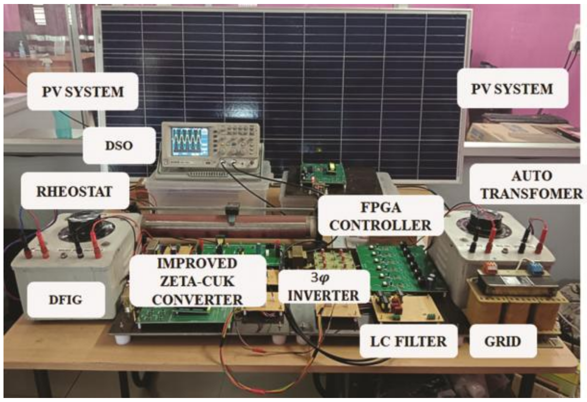

Fig. 24 — Experimental prototype.

Figure 27(a-b) display the waveform of DFIG and Rectifier. Despite minor distortions initially, DFIG consistently generates a stable AC output voltage. The rectifier proficiently transforms AC supply to a constant and stable DC voltage output of $600V$, ensuring steady power supply with minimal fluctuations.

Figure 28 depicts SOC of battery, revealing a recorded level of 60%. The SOC represents the proportion of the total battery capacity currently in use. In this instance, the visual representation signifies that the battery is operating at 60% of its full capacity, providing a clear indication of the current energy storage status.

Grid power dynamic waveforms is shown in Fig. 29(a-b). The proposed system achieves a stabilized

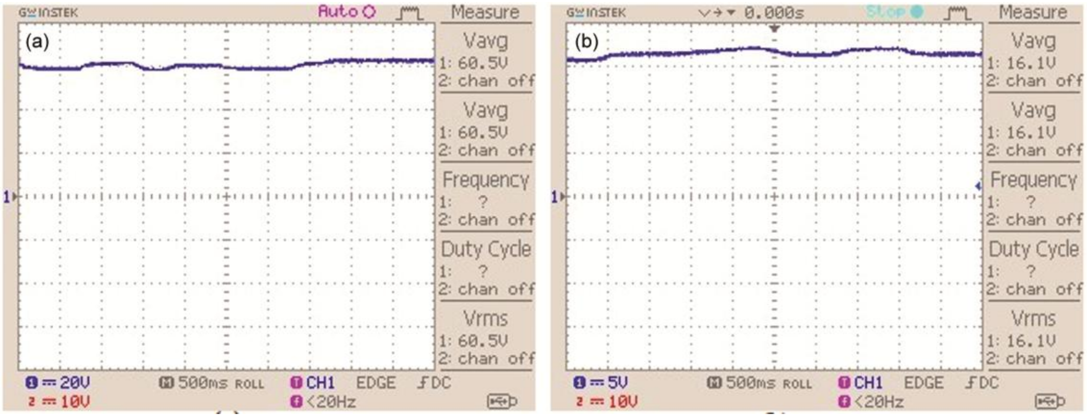

Fig. 25 — Solar PV panel characteristics (a) Voltage and (b) Current.

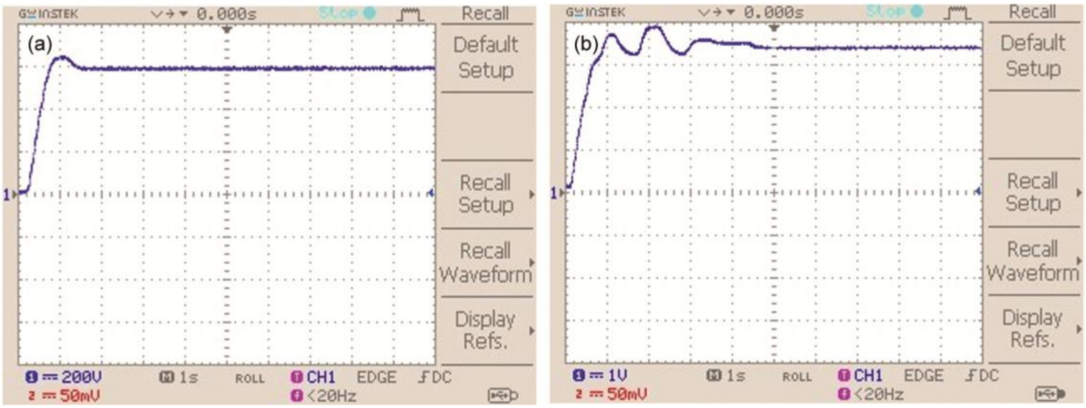

Fig. 26 —Representation of (a) IZC converter voltage and (b) Current.

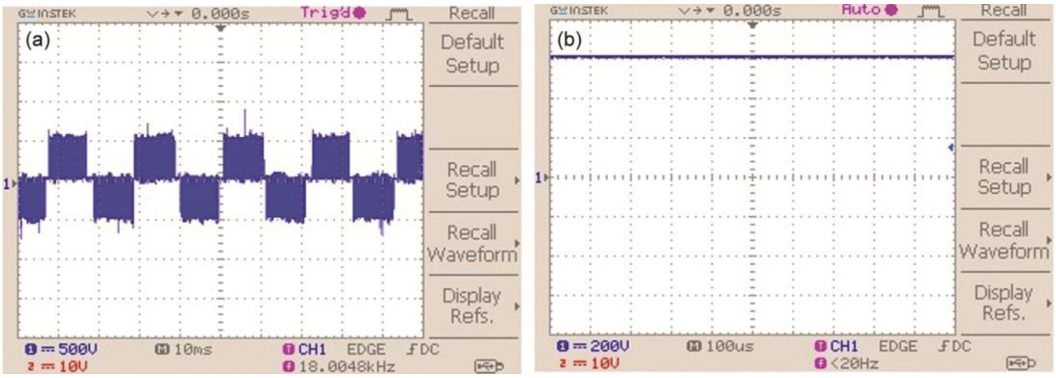

Fig. 27 — Wind characteristics (a) Output of DFIG and (b) Rectifier output.

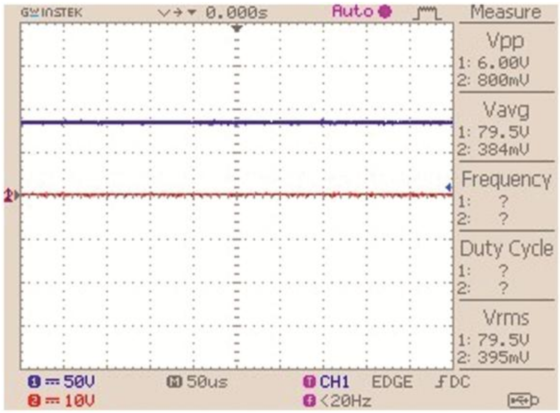

Fig. 28 — Battery SOC profile.

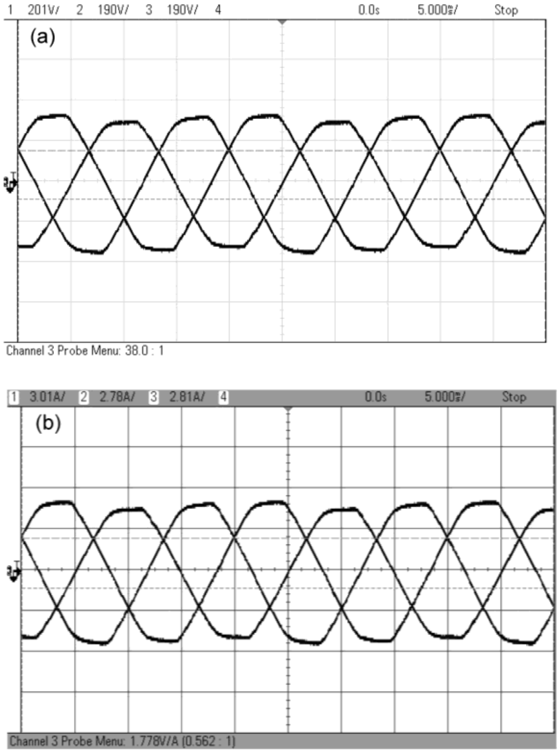

Fig. 29 — (a) Voltage and (b) Current at grid.

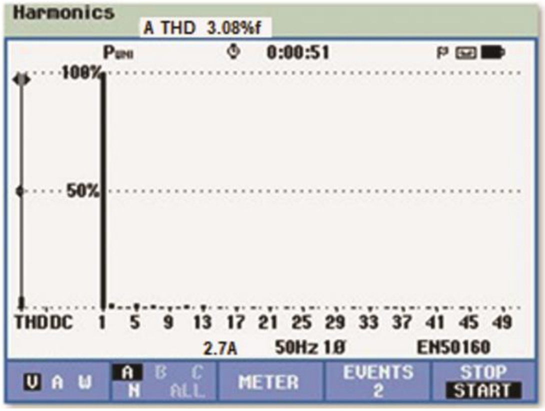

Fig. 30 — THD of grid current.

Table 5 — Comparison of converter analysis.

Converter	Efficiency (%)
Improved Boost Abouchabana[31]	92
Quadratic Modified SEPIC Esmaeili[32]	93
Switched Z-source Ahmad[33]	94.2
Diode Clamped Quasi Z-source Naderi[34]	94.8
Proposed Improved Zeta-Cuk	95.86

grid voltage and current, ensuring consistent and reliable electrical supply.

The grid current, revealing noteworthy information about the amount of harmonics existing in the system is shown in Fig. 30. The THD value of 3.08% signifies that 3.08% of the grid current is comprised of harmonic components relative to the fundamental frequency. This indicates a moderate level of harmonic distortion in grid current waveform.

The efficiency performance of different converters, each playing a crucial role in energy conversion is listed in Table 5. The presented converters include the Improved Boost Abouchabana[31] with an efficiency of 92%, Quadratic Modified SEPIC Esmaeili[32] possess an efficiency of 93%, Switched Z-source Ahmad[33] achieving an efficiency of 94.2%, and Diode Clamped Quasi Z-source Naderi[34] with an efficiency of 94.8%.

Notably, the Proposed IZC converter stands out with a remarkably high efficiency of 95.86% suggesting its potential as an optimized solution for energy conversion applications, with enhanced performance and reduced energy losses compared to the other converters in the comparison. In addition, Fig. 31(a) visualizes the graphical representation of converter efficiency.

Analysis of various MPPT techniques based on their Tracking Efficiency, is expressed in percentage and listed in Table 6, with its graphical representation in Fig. 31(b). The evaluated MPPT techniques include PIOZhao[35] with a tracking efficiency of 92.77%, Variable Step In Cond Zakzouk[36] with 96%, EA Mendez[37] with 96.25%, and M-FireflyLi[38]with 97.13% tracking efficiency. Notably, the Proposed Cascaded ANFIS emerges as the frontrunner, achieving an impressive tracking efficiency of 97.8%, harvesting capabilities of PV system compared to other evaluated techniques.

Figure 32(a) presents a detailed breakdown of power losses in the IZC converter. The power loss components include switching loss (36%), which accounts for losses during semiconductor transitions; capacitor loss (14%), representing energy dissipation in capacitive elements; inductor loss (15%), resulting from resistance in inductive components; and diode loss (35%), encompassing conduction and recovery losses in diode components. This breakdown offers a comprehensive understanding of where and how losses occur, aiding in targeted optimization efforts to enhance the overall efficiency of the IZC Converter.

Simultaneously, Fig. 32(b) illustrates the efficiency versus output power characteristics of IZC Converter. As the output power increases from 2000W to 10,000W, the converter demonstrates a remarkable improvement in efficiency. Starting at 85.36% for 2000W, the efficiency consistently rises, reaching 89% at 4000W, 92.10% at 6000W, 95% at 8000W and achieves a high efficiency of 95.86% for 10000W. This trend underscores the IZC converter's ability to maintain high efficiency levels across a range of output power values, indicating its effectiveness in converting electrical power with minimal losses, particularly at higher power levels.

Table 6 — Performance analysis of tracking efficiency.

MPPT Techniques	Tracking Efficiency (%)
PIO Zhao[35]	92.77
Variable Step In Cond Zakzouk[36]	96
EA Mendez[37]	96.25
M-firefly Li[38]	97.13
Proposed Cascaded ANFIS	97.8

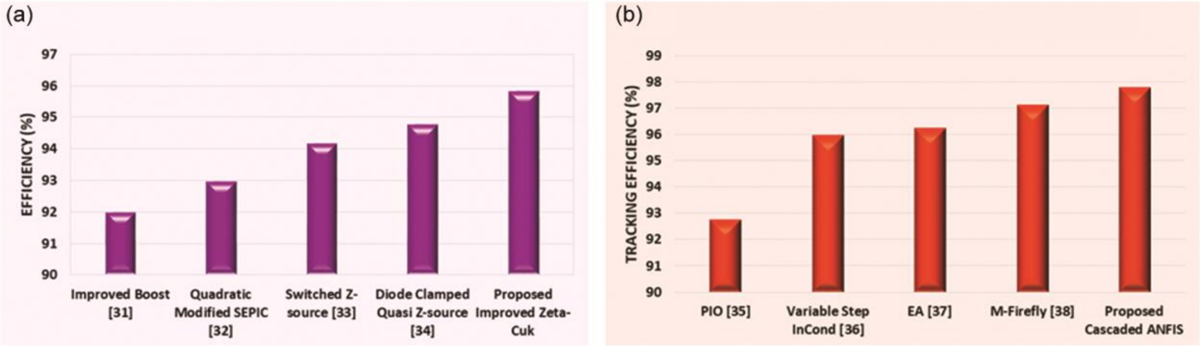

Fig. 31 — Assessment on (a) Converter efficiency and (b) Efficiency of MPPT method.

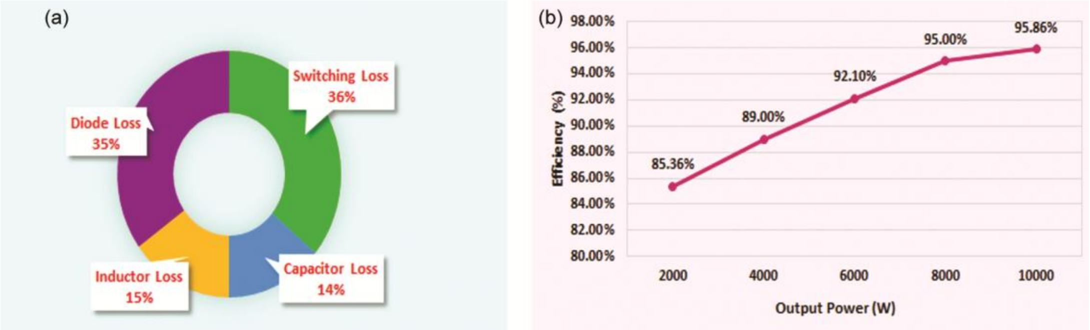

Fig. 32 — Assessment of (a) Power loss breakdown and (b) Efficiency versus output power.

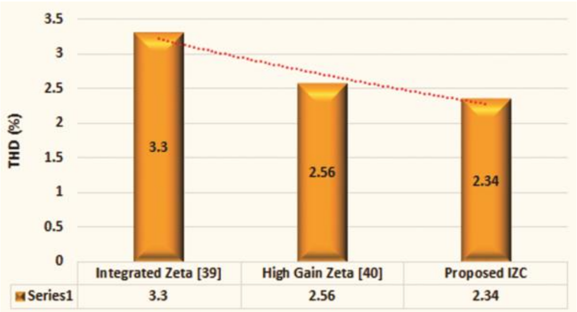

Fig. 33 — Comparative analysis of THD.

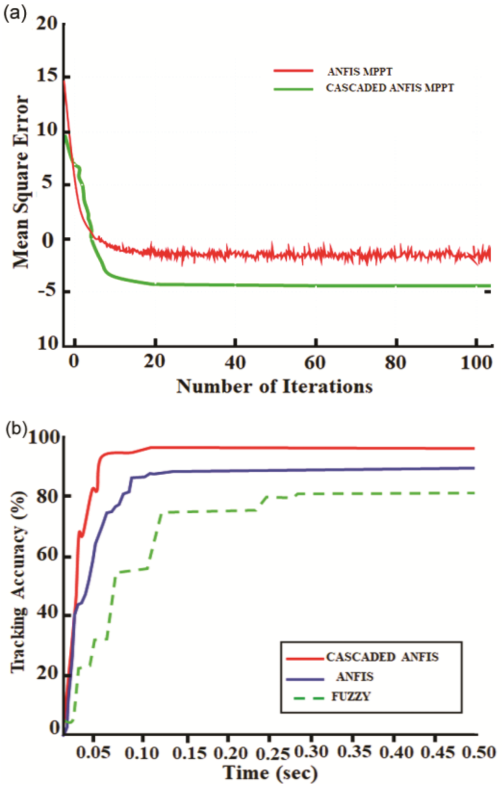

Fig. 34 — Analysis of (a) Mean square error and (b) Tracking performance.

Figure 33 compares the THD values for different converter designs, including Integrated Zeta Dionizio[39] with THD of 3.3% and High Gain Zeta Pattathurani[40]with THD of 2.56%. Particularly, the Proposed IZC Converter with a significantly lower THD of 2.34% indicating reduced harmonic components in the output waveform, highlighting superior distortion-minimizing performance.

The error measure of MPPT is analysed for conventional ANFIS and cascaded ANFIS, shown in Fig. 34(a). From the comparison it is witnessed that, the cascaded ANFIS shows minimized error in contrast to conventional ANFIS MPPT, foreshowing the performance of proposed technique.

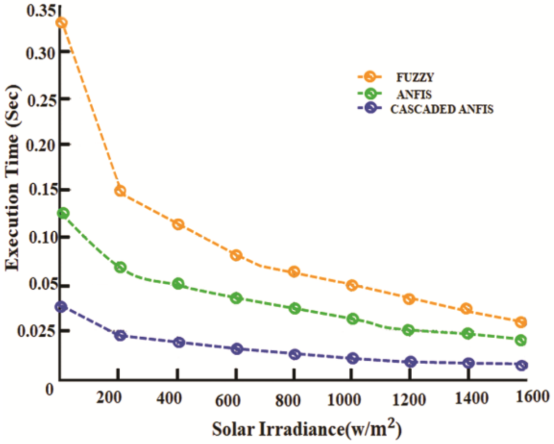

Fig. 35 — Execution time of evaluation.

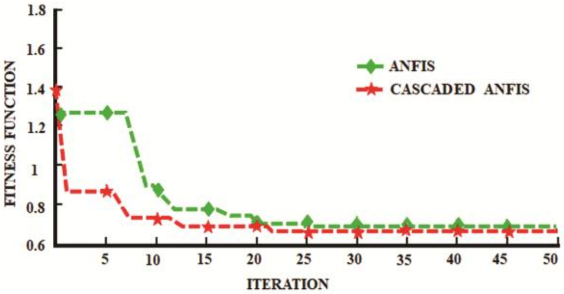

Fig. 36 — Comparison of fitness function versus iteration.

Simultaneously, in Fig. 34(b) the tracking ability is portrayed, showing the superior performance of cascaded ANFIS MPPT, with tracking accuracy of 96.2% in contrast to traditional Fuzzy and ANFIS techniques.

The comparative analysis of various MPPT controller is illustrated in Fig. 35 to predict the optimal approach in response with execution time. The assessment is made between fuzzy, ANFIS and the proposed Cascaded ANFIS approach. The Figure makes clear that the proposed cascaded ANFIS approach ranks with faster execution time in contrast to other similar MPPT techniques.

Figure 36 depicts fitness functions assessment for ANFIS MPPT and Cascaded ANFIS MPPT. The graph illustrates the optimization process for both techniques, showcasing their performance over successive iterations. Through the comparison, the proposed Cascaded ANFIS MPPT demonstrates an improved fitness function compared to the conventional ANFIS MPPT. This improvement implies that the Cascaded ANFIS MPPT converges more effectively toward the optimal solution, achieving better tracking of MPP with each iteration.

4 Conclusion

This research addresses the challenges posed by the increasing adoption of EVs by proposing an innovative solution: the integration of HRESs for EV charging. The fusion of solar, wind, and battery technologies, facilitated by IZC converter with Cascaded ANFIS for MPPT, stands out as a novel approach. Cascaded ANFIS MPPT algorithm foreshows superior performance by dynamically adjusting its parameters, leading to more precise and effective tracking of MPP of solar panel. The inclusion of DFIG in the wind system, controlled by PI controller, ensures stable voltage levels. MATLAB validation demonstrates an impressive converter efficiency of 95.86% and a noteworthy reduction in THD to 2.34%, confirming the efficiency and feasibility of proposed hybrid energy system, with enhanced voltage gain. Moreover, this work serves as a valuable contribution to the ongoing efforts in advancing sustainable and eco-friendly transportation coupled with energy management strategies.

References

1 Li Y, Han M, Yang Z &Li G, *IEEE Transac Sustain Ener*, 12(4) (2021) 2321.
2 Lenka R K, Panda A K, Patel R & Guerrero JM, *IEEE Transac Ind Appl*, 58(5) (2022) 5520.
3 Gomathi S, *2024 International Conference on Power, Energy, Control and Transmission Systems (ICPECTS)*, Chennai, India, (2024) 1.
4 Bekiroglu E & Esmer S, *Electr Power Compon Syst*, (2024) 1.
5 Kavin K S & Subha Karuvelam P, *IETE J Res*, (2021).
6 VelpulaS, Thirumalaivasan R & Janaki M, *IEEE Trans Power Syst*, 35(6) (2020) 4745.
7 Xia Y, Chen Y, Song Y & StrunzK, *IEEE Trans Energy Convers*, 35(1) (2019) 560.
8 Pires V F, Cordeiro A, Foito D & Silva JF, *IEEE Access*, 9 (2021) 157124.
9 Kumar R T & Rajan C C, *e-Prime-Adv Electr Eng, Electron Ene*, 6 (2023) 100347.
10 Preethy VK, Kumar R T, Radhika P, Nagarajan A, Faizal A M & Sasikumar M, In *2024 7th International Conference on Circuit Power and Computing Technologies (ICCPCT)*, 1 (2024) 534. IEEE.
11 Kumar R T, Balaji V, Sakthidhasan K, Gomathi S, Sreedhar R & Janaki N, In *2024 7th International Conference on Circuit Power and Computing Technologies (ICCPCT)*, 1 (2024) 540. IEEE.
12 Kumar R T, Sireesha G, Sakthidhasan K, Permila T R, Ramya R & Subasini PT, In *2024 2nd International Conference on Computer, Communication and Control (IC4)*, (2024) 1. IEEE.
13 Kumar R T & Rajan CC, *2024 IEEE Power & Energy Society General Meeting (PESGM)*, Seattle, WA, USA, (2024).
14 Zaoskoufis K & Tatakis EC, *IEEE J Emerg Sel Top Power Electron*, 9(2) (2020) 1837.
15 Shawky A, Takeshita T, Sayed M A, Aly M & Ahmed EM, *IEEE Access*, 9 (2021) 58689.
16 Veerachary M & Khuntia M R, *IEEE Trans Ind Electron*, 69(4) (2021) 3577.
17 Paul A R, Bhattacharya A & Chatterjee K, *IEEE Trans Ind Electron*, (2023).
18 Zeng Y, Li H, Wang W, Zhang B & Zheng TQ, *IEEE Trans Ind Electron*, 68(5) (2020) 3992.
19 Hosseini S H, Ghazi R & Heydari-Doostabad H, *IEEE Trans Ind Electron*, 68(6) (2020) 4859.
20 Ibrahim M H, Ang S P, Dani M N, Rahman M I, Petra R & Sulthan S M, *IEEE Access*, 11 (2023) 13079.
21 Bhan V, Shaikh SA, Khand Z H, Ahmed T, Khan L A, Chachar F A & Shaikh A M, *J Control Autom Electr Syst*, 32(6) (2021) 1652.
22 Gupta A K, Pachauri R K, Maity T, Chauhan Y K, Mahela O P, Khan B & Gupta P K, *IEEE Access*, 9 (2021) 90977.
23 Ali A I, Mousa H H, Mohamed H R, Kamel S, Hassan A S, Alaas Z M, Mohamed E E & Abdallah AR, *IEEE Access*, (2023).
24 Allahabadi S, Iman-Eini H & Farhangi S, *IEEE Trans Ind Electron*, 69(6) (2021) 5879.
25 Subramanian V, Indragandhi V, Kuppusamy R & Teekaraman Y, *Electronics*, 10(20) (2021) 2541.
26 Ibrahim S A, Nasr A & Enany M A, *IEEE Access*, 9 (2021) 114457.
27 Kraiem H, Flah A, Mohamed N, Alowaidi M, Bajaj M, Mishra S, Sharma N K & Sharma S K, *IEEE Access*, 9 (2021) 72040.
28 Abadlia I, Hassaine L, Beddar A, Abdoune F & Bengourina MR, *Int J Hydrogen Ener*, 45(43) (2020) 22589.
29 Huang K H, Chao K H & Lee T W, *Technologies*, 11(2) (2023) 61.
30 Guo K, Cui L, Mao M, Zhou L & Zhang Q, *IEEE Access*, 8 (2020) 103476.
31 Abouchabana N, Haddadi M, Rabhi A, Grasso A D &Tina GM, *Appl Sci*, 11(3) (2021) 980.
32 Esmaeili S, Shekari M, Rasouli M, Hasanpour S, Khan AA & Hafezi H, *IEEE Trans Ind Applic*, (2023).
33 Ahmad A, Singh R K & Beig A R, *IEEE Access*, 7 (2019) 179918.
34 Naderi S & Rastegar H, *IEEE Access*, 11 (2023) 2941.
35 Zhao Z, Zhang M, Zhang Z, Wang Y, Cheng R, Guo J, Yang P, Lai C S, Li P & Lai LL, *IEEE Trans Ind Electron*, 69(10) (2021) 10129.
36 Zakzouk N E, Elsaharty M A, Abdelsalam A K, Helal A A & Williams B W, *IET Renew Power Gener*, 10(4) (2016) 561.
37 Mendez E, Ortiz A, Ponce P, Macias I, Balderas D & Molina A, *Energies*, 13(12) (2020) 3047.
38 Li W, Zhang G, Pan T, Zhang Z, Geng Y & Wang J, *IEEE Access*, 7 (2019) 126323.
39 Dionizio A A, Sampaio L P, da Silva S A & Machado S D, *Energies*, 16(9) (2023) 3622.
40 Pattathurani L P, Dash S S, Dwibedi R K, Raj M D, Kannadasan R, Savio M F, Alsharif M H & Kim J H, *Sustainability*, 14(12) (2022) 7028.